

Regulation of the pancreatic K_{ATP} channel

Samuel Usher

Green Templeton College
University of Oxford

*A thesis submitted for the degree of
Doctor of Philosophy*

Trinity 2021

Abstract

Regulation of the pancreatic K_{ATP} channel



Samuel Usher
Green Templeton College
University of Oxford

A thesis submitted for the degree of

Doctor of Philosophy

Trinity 2021

Acknowledgements

Abstract

Contents

List of Figures	ix
1 Introduction	1
1.1 General introduction	1
1.2 Structure and function of the pancreatic K _{ATP} channel	1
1.2.1 Pancreatic islets and the β-cell	1
1.2.2 Glucose induced insulin secretion in β-cells	2
1.2.3 Architecture of the pancreatic K _{ATP} channel	2
1.2.4 Nucleotide regulation of the pancreatic K _{ATP} channel	4
1.3 Fluorescence methods in ion channel research	5
1.3.1 Fluorescence as a tool	5
1.3.2 Forster resonance energy transfer	5
1.3.3 Unnatural amino acid incorporation	5
1.4 Functional modelling of ion channels	5
1.4.1 Why?	5
1.4.2 A model that fits	5
2 Methods	9
2.1 Molecular biology	9
2.2 Cell culture and channel expression	10
2.3 Western blots	11
2.4 Confocal microscopy	12
2.5 Surface expression assays	13
2.6 Epifluorescence imaging and spectroscopy	14
2.7 Electrophysiology	14
2.8 FRET calculations	15
2.9 Unroofed binding measurements	16
2.10 Patch-clamp fluorometry	17
2.11 Data processing and presentation	17
2.12 Computational docking	18
2.13 Chemicals and stock solutions	19

3 Measuring nucleotide binding to K_{ATP}	21
3.1 Choosing a site to incorporate Anap	21
3.1.1 Scanning a region	21
3.1.2 Rational residues	22
3.2 Testing for membrane expression	22
3.2.1 Expression with SUR1	22
3.2.2 Expression alone/with TMD0(195/232)	23
4 MWC model formulation	25
4.1 The MWC model	25

Appendices

List of Figures

1.1	Structure of Kir6.2	3
1.2	Structure of SUR1	5
1.3	K _{ATP} architecture and nucleotide regulation	6
1.4	SUR1 intrinsically modulates Kir6.2	7
3.1	Anap and TNP-nucleotides as FRET pairs	22
4.1	Single ligand, single protomer	26
4.2	Two non-interacting ligands, single protomer	27

x

1

Introduction

Contents

1.1 General introduction	1
1.2 Structure and function of the pancreatic K_{ATP} channel	1
1.2.1 Pancreatic islets and the β-cell	1
1.2.2 Glucose induced insulin secretion in β-cells	2
1.2.3 Architecture of the pancreatic K _{ATP} channel	2
1.2.4 Nucleotide regulation of the pancreatic K _{ATP} channel	4
1.3 Fluorescence methods in ion channel research	5
1.3.1 Fluorescence as a tool	5
1.3.2 Förster resonance energy transfer	5
1.3.3 Unnatural amino acid incorporation	5
1.4 Functional modelling of ion channels	5
1.4.1 Why?	5
1.4.2 A model that fits	5

1.1 General introduction

1.2 Structure and function of the pancreatic K_{ATP} channel

1.2.1 Pancreatic islets and the β-cell

Pancreatic islets are endocrine cells which are responsible for maintaining glucose homeostasis. There are roughly one million islets in a human pancreas, constituting

1-2% of the total pancreatic mass. Islets consist of three principal cell types; insulin secreting β -cells, glucagon secreting α -cells and somatostatin secreting δ -cells. Islets respond to increases in blood glucose by releasing insulin, which acts on peripheral tissues to increase glucose uptake and reduce blood glucose levels. Conversely, decreases in blood glucose leads to the release of glucagon, which acts on those tissues to stimulate glucose production and increase blood glucose.

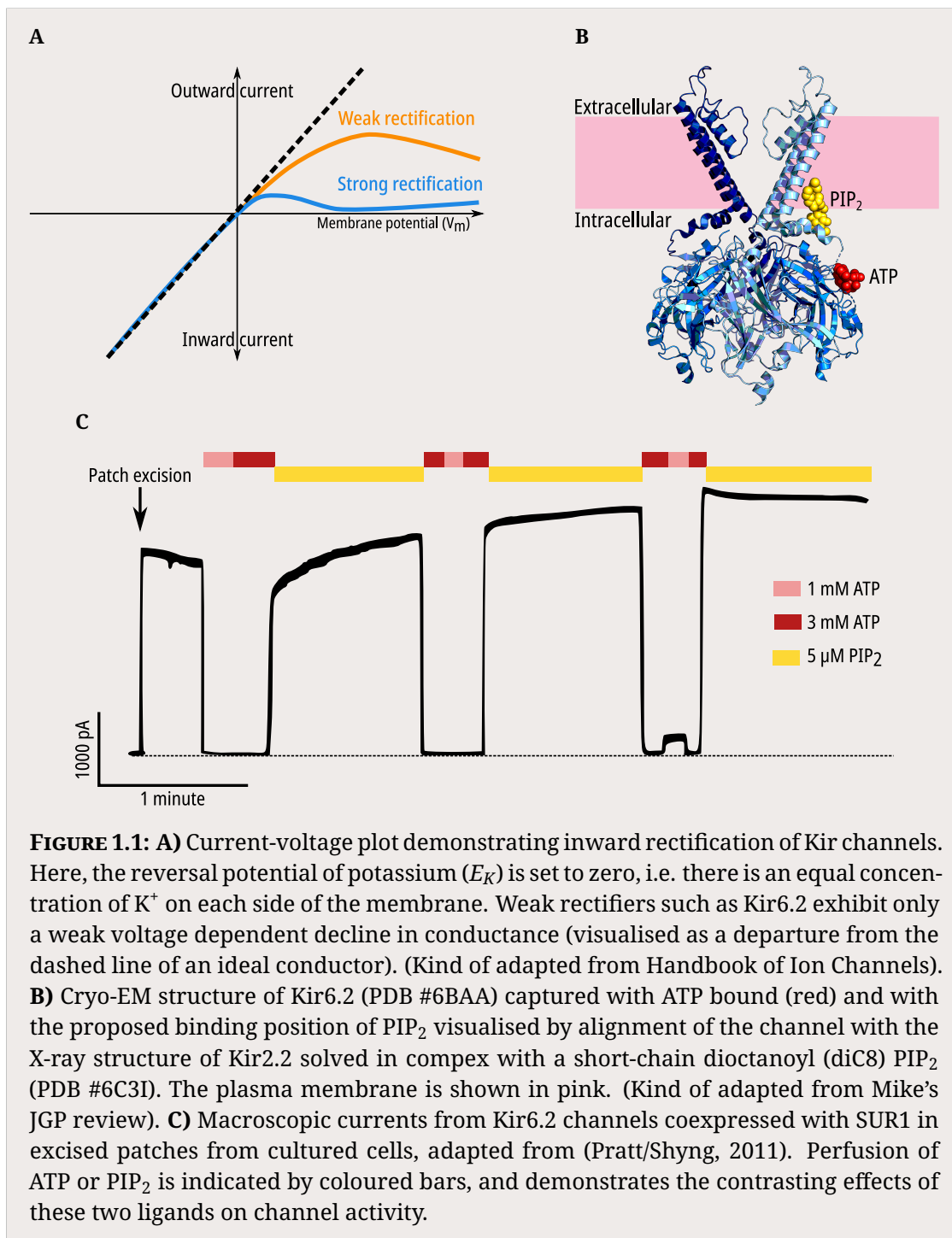
1.2.2 Glucose induced insulin secretion in β -cells

1.2.3 Architecture of the pancreatic K_{ATP} channel

ATP-sensitive potassium (K_{ATP}) channels are present in many tissues, where they couple the metabolic state of a cell to its electrical activity by regulating the flow of K⁺ across the membrane. K_{ATP} channels are an octameric complex, comprised of four inwardly-rectifying potassium channel subunits (Kir6.1 or Kir6.2), each of which is associated with a sulphonylurea receptor subunit (SUR1, SUR2A or SUR2B). In pancreatic β -cells, the K_{ATP} channel isoform is composed of Kir6.2 and SUR1.

Inwardly-rectifying potassium channels are so named because they allow K⁺ to flow more easily into the cell than out of it (Figure 1.1A). This phenomenon is a consequence of voltage-dependent pore blockade by intracellular divalent cations (especially Mg²⁺) and polyamines. At depolarising membrane potentials, blockers are driven into the pore and K⁺ current is blocked, while at hyperpolarising potentials the blockers are cleared and K⁺ current can flow. Strongly rectifying Kir channels display drastically reduced conductance at potentials more positive than the K⁺ reversal potential. In contrast, Kir6.2 is a weak rectifier, and allows substantial current to flow at more positive potentials.

In addition to voltage, Kir6.2 is regulated by two endogenous ligands; phosphatidylinositol 4,5-bisphosphate (PIP₂) and adenine nucleotides (Figure 1.1B). The binding of adenine nucleotides to Kir6.2 leads to closure of the channel pore, while the binding of PIP₂ promotes the opening of the pore (Figure 1.1C). Activation by PIP₂ is a mechanism common to the whole Kir family, whereas inhibition by nucleotides is unique to the Kir6 subfamily.



SUR1 is a member of the ATP-binding cassette (ABC) family of transporters. While other ABC proteins transport substrate across the membrane, SUR1 does not appear to do so; instead it acts to modulate the function of its associated ion channel. The cystic fibrosis transmembrane conductance regulator (CFTR) is another

member of the ABC family, and is an ion channel in its own right, capable of conducting chloride across the membrane. Like other ABC proteins, SUR1 contains two sets of transmembrane domains (TMD1 and TMD2) and two cytosolic nucleotide binding domains (NBD1 and NBD2). Unique to SUR is the presence of an additional transmembrane domain (TMD0) N-terminal to the core of the protein, and this domain forms the primary contact between SUR1 and Kir6.2.

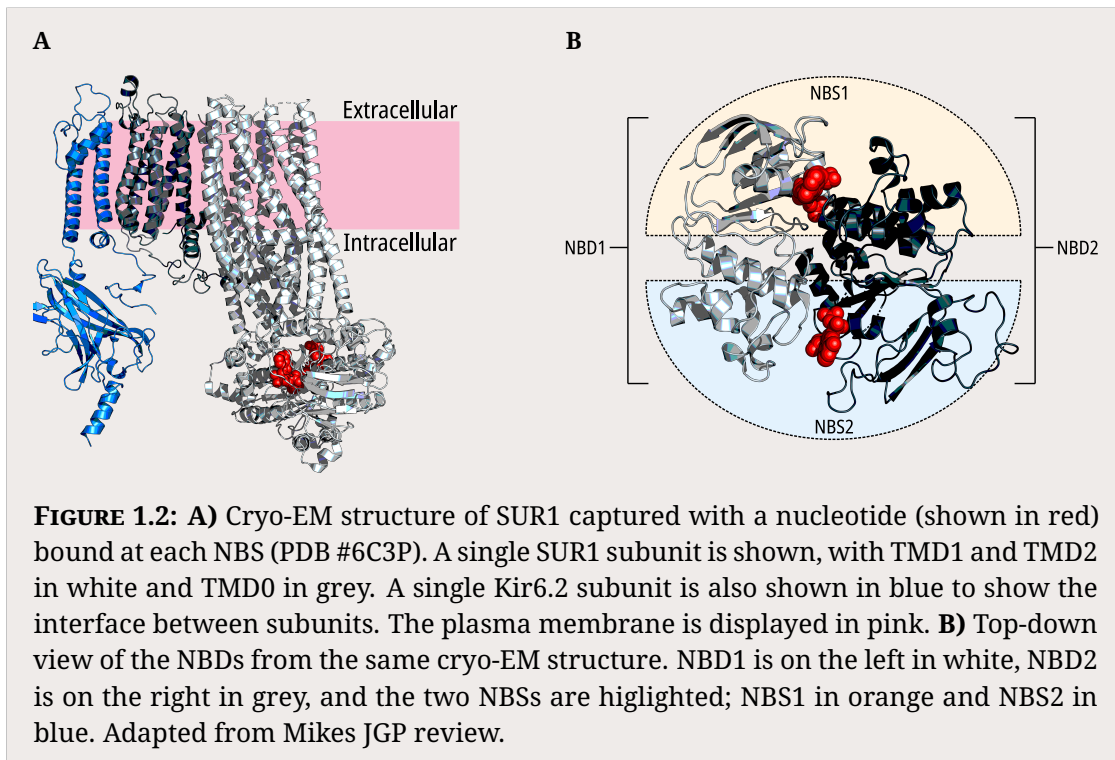
The NBDs of ABC transporters are highly conserved, and consist of two subdomains: a larger RecA-like subdomain found in other P-loop ATPases, and a smaller α -helical subdomain which is unique to ABC transporters. There are three key structural motifs present in these subdomains: the RecA-like subdomain contains the Walker A (W_A) and B (W_B) motifs, while the α -helical subdomain contains the ABC signature motif (typically LSGGQ).

The two domains come together to form an antiparallel dimer with two nucleotide binding sites (NBS1 and NBS2) at the interface, such that NBS1 is formed from the W_A and W_B motifs of NBD1 and the signature motif from NBD2, whereas NBS2 is formed from the W_A and W_B motifs of NBD2 and the signature motif from NBD1. NBS2, also known as the consensus site as it is more similar in sequence to other ABC family members, is catalytically competent and able to hydrolyse ATP. In contrast, NBS1 is the degenerate site, with a less conserved sequence and an inability to catalyse hydrolysis of ATP.

Sulphonylureas go here.

1.2.4 Nucleotide regulation of the pancreatic K_{ATP} channel

Together, Kir6.2 and SUR1 form a complex nearly a megadalton in size and over 15 nanometres across (Figure 1.3A, 1.3B). While the binding of adenine nucleotides to the Kir6.2 binding site leads to closure of the pore, binding of nucleotides to either of the two NBSs of SUR1 in the presence of Mg²⁺ activates the channel. The interplay between the action of nucleotides at these distinct sites (Figure 1.3C) determines the response of the K_{ATP} channel to metabolic changes, and therefore even subtle mutations or modifications to these sites can lead to diseases of insulin secretion.



In addition to its nucleotide binding and sensitivity to sulphonylureas, SUR1 also has intrinsic effects on channel properties. The presence of SUR1 increases the open probability of the channel pore (Figure 1.4A), and this increase is conferred by the TMD0 region (Figure 1.4B). Furthermore, coexpression of SUR1 increases the sensitivity of Kir6.2 to inhibition by nucleotides (Figure 1.4C).

1.3 Fluorescence methods in ion channel research

1.3.1 Fluorescence as a tool

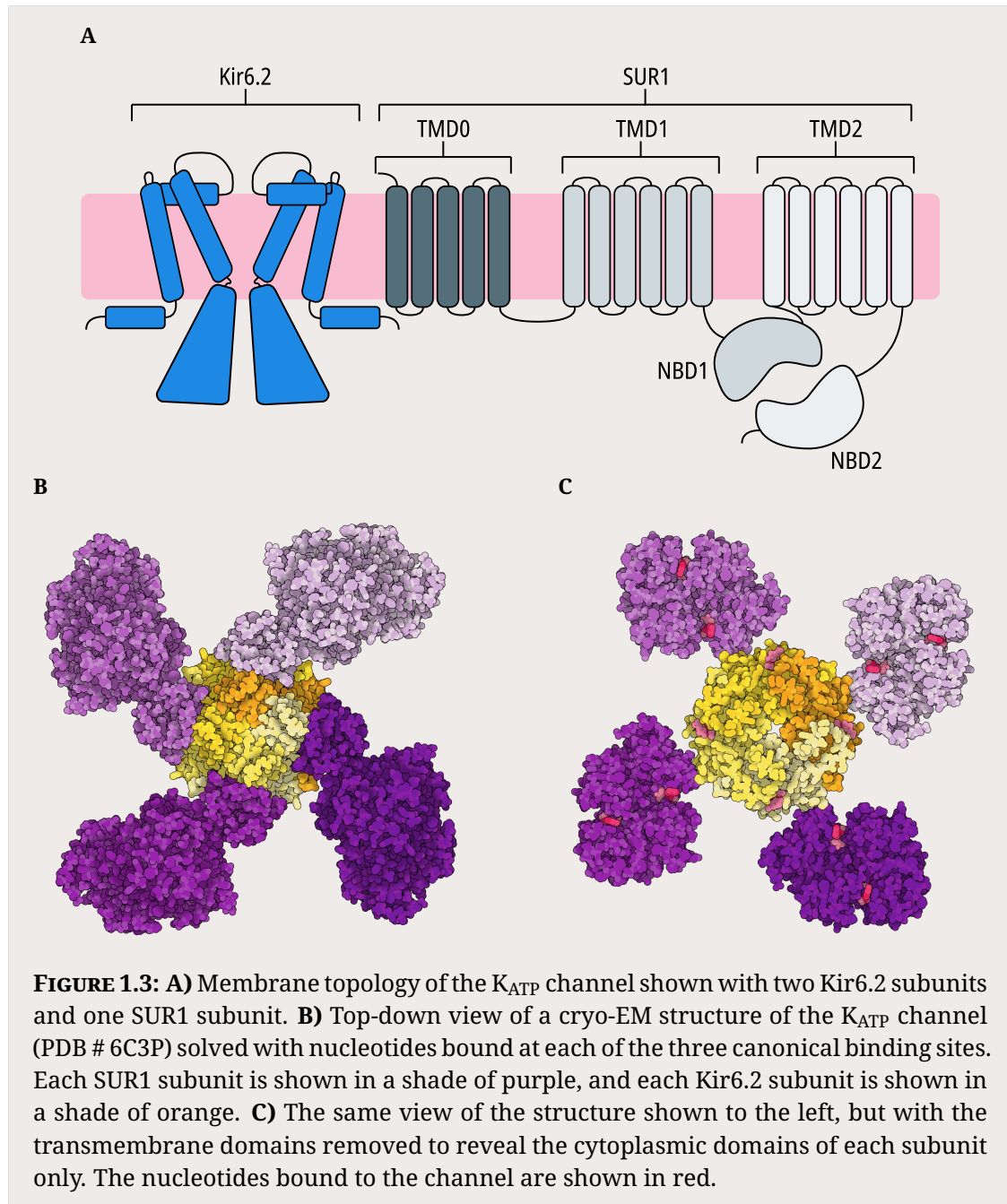
1.3.2 Forster resonance energy transfer

1.3.3 Unnatural amino acid incorporation

1.4 Functional modelling of ion channels

1.4.1 Why?

1.4.2 A model that fits



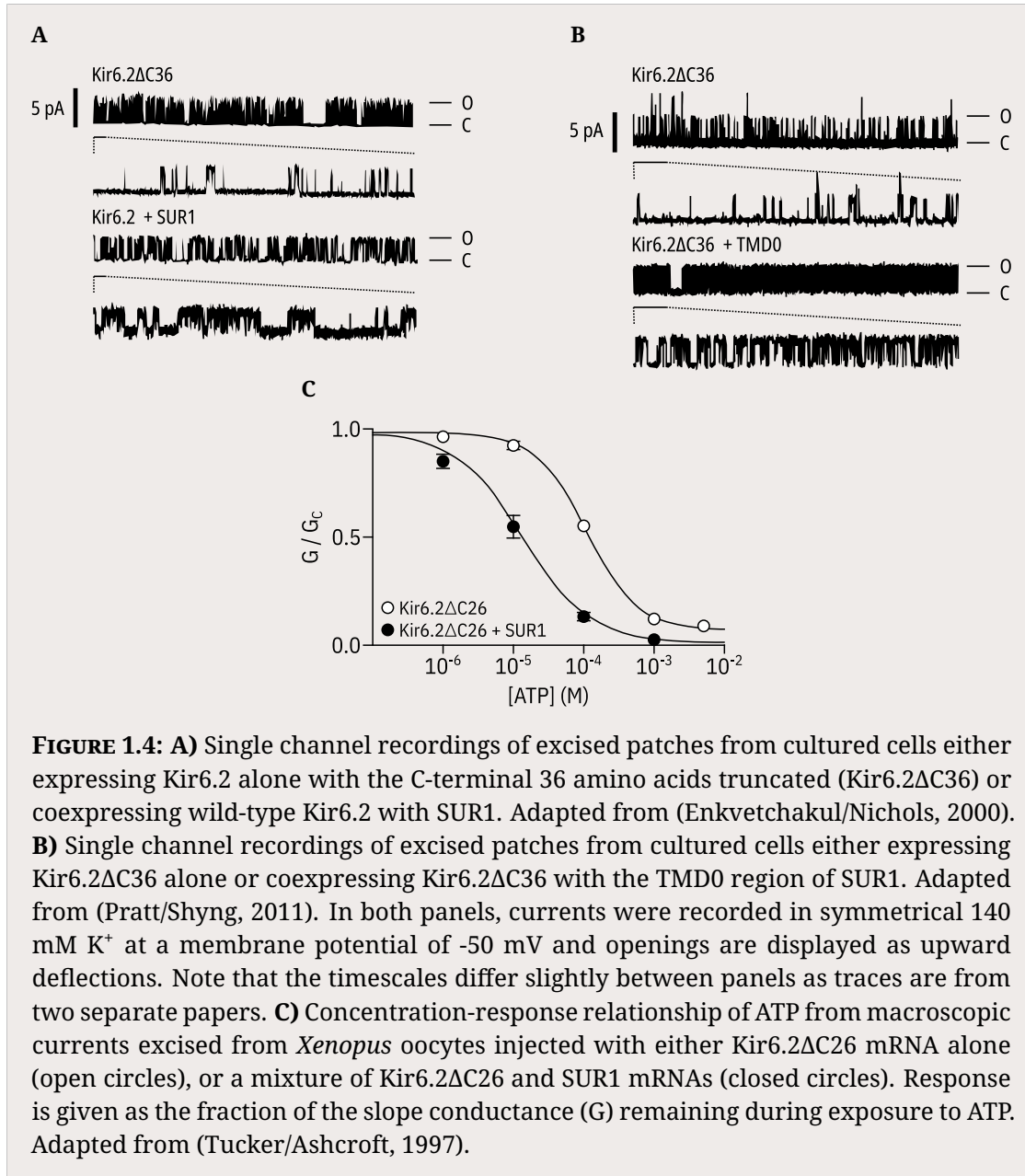


FIGURE 1.4: **A)** Single channel recordings of excised patches from cultured cells either expressing Kir6.2 alone with the C-terminal 36 amino acids truncated (Kir6.2ΔC36) or coexpressing wild-type Kir6.2 with SUR1. Adapted from (Enkvetchakul/Nichols, 2000). **B)** Single channel recordings of excised patches from cultured cells either expressing Kir6.2ΔC36 alone or coexpressing Kir6.2ΔC36 with the TMD0 region of SUR1. Adapted from (Pratt/Shyng, 2011). In both panels, currents were recorded in symmetrical 140 mM K⁺ at a membrane potential of -50 mV and openings are displayed as upward deflections. Note that the timescales differ slightly between panels as traces are from two separate papers. **C)** Concentration-response relationship of ATP from macroscopic currents excised from *Xenopus* oocytes injected with either Kir6.2ΔC26 mRNA alone (open circles), or a mixture of Kir6.2ΔC26 and SUR1 mRNAs (closed circles). Response is given as the fraction of the slope conductance (G) remaining during exposure to ATP. Adapted from (Tucker/Ashcroft, 1997).

2

Methods

Contents

2.1 Molecular biology	9
2.2 Cell culture and channel expression	10
2.3 Western blots	11
2.4 Confocal microscopy	12
2.5 Surface expression assays	13
2.6 Epifluorescence imaging and spectroscopy	14
2.7 Electrophysiology	14
2.8 FRET calculations	15
2.9 Unroofed binding measurements	16
2.10 Patch-clamp fluorometry	17
2.11 Data processing and presentation	17
2.12 Computational docking	18
2.13 Chemicals and stock solutions	19

2.1 Molecular biology.

Human Kir6.2 and SUR1 were subcloned into pcDNA4/TO and pCGFP_EU vectors for expression of wild-type and GFP-tagged constructs, respectively. pcDNA4/TO and pANAP were obtained from Addgene. peRF1-E55D and pCGFP_EU were kind gifts from the Chin Laboratory (MRC Laboratory of Molecular Biology, Cambridge, UK) and the Gouaux Laboratory (Vollum Institute, Oregon, USA) respectively. Amber

stop codons and point mutations were introduced using the QuikChange XL system (Stratagene; San Diego, CA). All constructs were confirmed by DNA sequencing (DNA Sequencing and Services, University of Dundee, Scotland).

2.2 Cell culture and channel expression

HEK-293T cells were obtained from and verified/tested for mycoplasma by LGC standards (ATTC CRL-3216, Middlesex, UK). Our working stock tested negative for mycoplasma contamination using the MycoAlert Mycoplasma Detection Kit (Lonza Bioscience; Burton on Trent, UK). Cells were plated onto either poly-L-lysine coated borosilicate glass coverslips (VWR International; Radnor, PA) or poly-D-lysine coated glass-bottomed FluoroDishes (FD35-PDL-100, World Precision Instruments). ANAP-tagged Kir6.2 constructs were labelled using amber stop codon suppression as described by Chatterjee et al. Transfections were carried out 24 hours after plating using TransIT-LT1 (Mirus Bio LLC; Madison, WI) at a ratio of 3 µl per µg of DNA. Unless specified otherwise, all transfections included a Kir6.2 construct with an amber stop codon (TAG) at position 311 (Kir6.2-W311^{TAG}), SUR1, pANAP and eRF1-E55D in the ratio 0.5:1.5:1:1. Transfected cells cultured in Dulbecco's Modified Eagle Medium (Sigma; St. Louis, MO) + 10% foetal bovine serum, 100 U ml⁻¹ penicillin and 100 µg ml⁻¹ streptomycin (Thermo Fisher Scientific; Waltham, MA) supplemented with 20 mM ANAP (free acid, AsisChem; Waltham, MA). Cells were incubated at 33 °C and in the presence of 300 µM tolbutamide to enhance protein expression and channel trafficking to the plasma membrane. eRF1-E55D was included to increase efficiency of ANAP incorporation. Experiments were carried out 2-4 days after transfection. We also expressed constructs labelled with ANAP at positions I182, F183, F198, and I210. Kir6.2-F183*, Kir6.2-F198*, and Kir6.2-I210* co-expressed with SUR1 did not produce sufficient currents for subsequent experimentation. Mutations at I182 are known to produce profound effects on nucleotide inhibition of K_{ATP}. Thus, we did not consider this site for further experimentation.

2.3 Western blots

Transfected HEK-293T cells grown in 6-well plates were harvested in cold PBS (Life Technologies Limited; Paisley, UK), pelleted at 0.2 x g for 2.5 minutes and resuspended in lysis buffer containing 0.5% Triton X-100, 100 mM potassium acetate, and a cOmplete protease inhibitor tablet (1 tablet/50 ml, Roche; Basel, Switzerland), buffered to pH 7.4. After a 30-minute benzonase (Sigma) treatment at room temperature, samples were mixed with a DTT containing reducing agent and loading buffer (NuPAGE, Invitrogen; Carlsbad, CA) and run on a precast Bis-Tris 4-12% polyacrylamide gel at 200 V for 40 minutes. Proteins were wet transferred overnight onto polyvinylidene difluoride (PVDF) membranes (Immobilon P, Merck Millipore; Burlington, VT) in 25 mM Tris, 192 mM glycine, 20% methanol, and 0.1% SDS at 10 V on ice. Membranes were blocked with 5% milk in TBS-Tw (150 mM NaCl, 0.05% Tween 20, 25 mM Tris, pH 7.2) before staining for 30 minutes with a 1:1000 dilution of rat anti-HA monoclonal antibody in TBS-Tw (clone 3F10, Roche). After washing with TBS-Tw, membranes were incubated for 30 minutes with a 1:20,000 dilution of HRP-conjugated goat anti-rat polyclonal antibodies in TBS-Tw (Jackson ImmunoResearch; Ely, UK). Detection was performed using the SuperSignal West Pico Chemiluminescent Substrate (Thermo Fisher) and a C-DiGit Blot Scanner (Licor Biosciences; Lincoln, NE). Analysis was performed using custom code written in Python.

To confirm our ability to express full-length Kir6.2*-GFP, we performed western blots for HA-tagged Kir6.2 constructs in detergent-solubilized HEK-293T cells (Figure 1—Figure supplement 1C). The HA tag plus a short linker (YAYMEKGITDLAYPYD-VPDY) was inserted in the extracellular region following helix M1 of Kir6.2 between L100 and A101. Transfection of wild-type Kir6.2-HA or Kir6.2-HA-GFP resulted in two bands on the western blots. The upper bands were close to the expected sizes for full-length Kir6.2-HA and Kir6.2-HA-GFP (46 kDa and 77 kDa, respectively).

We consistently observed a lower molecular weight band as well. This band must correspond to an N-terminally truncated Kir6.2 product, as the apparent molecular weight shifted with addition of the C-terminal GFP tag. Based on the

molecular weight, we predict that the truncated protein product initiated from a start codon in the first transmembrane domain. Therefore, we believe it is unlikely that this protein would form functional channels or traffic to the plasma membrane. When Kir6.2-W311^{TAG}-HA or Kir6.2-W311^{TAG}-HA-GFP were co-transfected with SUR1, pANAP, and eRF1-E55D, and cells were cultured in the presence of ANAP, the western blots were similar to wild-type Kir6.2-HA or Kir6.2-HA-GFP. Over 90% full-length Kir6.2*-HA-GFP was produced under these conditions (Figure 1—Figure supplement 1D). We were unable to quantify the percentage of full-length Kir6.2*-HA produced as the C-terminally truncated band resulting from termination at the TAG codon was very similar in size to the N-terminally truncated band. Co-expression with SUR1 increased the percentage of full-length Kir6.2*-HA-GFP produced (Figure 1—Figure supplement 1D). In the absence of ANAP, we did not observe any full-length Kir6.2, indicating that there was no read-through of the amber (TAG) stop codon (Figure 1—Figure supplement 1D).

2.4 Confocal microscopy

Confocal imaging was performed using a spinning-disk system (Ultra-VIEW VoX, PerkinElmer; Waltham, MA) mounted on an IX81 microscope (Olympus; Southend-on-Sea, UK) with a Plan Apo 60x oil immersion objective (NA = 1.4), provided by the Micron Advanced Bioimaging Unit, Oxford. Transfected HEK-293T cells were incubated for 15 minutes with 1 nM CellMask Deep Red (Thermo Fisher) to stain plasma membranes before washing with PBS and imaging. ANAP was excited with a solid-state laser at 405 nM. GFP and CellMask were excited with an argon laser at 488 nM and 633 nM respectively. Images were captured on an EMCCD camera (ImagEM; Hamamatsu Photonics; Welwyn Garden City, UK) binned at 2 x 2 pixels and analysed using Python. A median filter with a box size of 32 x 32 pixels was applied to improve the signal-to-noise ratio by reducing background fluorescence.

We examined the surface expression of our ANAP-labelled constructs using confocal microscopy (Figure 1—Figure supplement 1A,B). When Kir6.2-W311^{TAG}-GFP was co-transfected with SUR1 along with pANAP and eRF1-E55D in the presence

of ANAP, the ANAP and GFP fluorescence were co-localized at the plasma membrane. When wild-type Kir6.2-GFP was transfected under the same conditions, only GFP fluorescence was observed at the plasma membrane. ANAP fluorescence was diffuse and confined to the cytoplasm or intracellular structures. Thus, the plasma-membrane ANAP signal was specific for Kir6.2*-GFP.

2.5 Surface expression assays

We measured surface expression of HA-tagged Kir6.2 subunits using an approach outlined by Zerangue et al. Cells were plated on 19 mm coverslips coated with poly-L-lysine and transfected as described above. Following incubation, cells were rinsed with PBS before fixation with 10% formalin for 30 minutes at room temperature. After washing again, cells were blocked with 1% BSA in PBS for 30 minutes at 4 °C before a 1-hour incubation at 4 °C with a 1:1000 dilution (in PBS) of rat anti-HA monoclonal antibodies. Cells were then washed 5 times on ice with 1% BSA in PBS followed by a 30-minute incubation at 4 °C with a 1:2000 dilution of HRP-conjugated goat anti-rat polyclonal antibodies. Cells were washed 5 times in PBS + 1% BSA and 4 times in PBS. Coverslips were removed from the culture dishes and placed in clean, untreated dishes for measurement. 300 µl of SuperSignal ELISA Femto Maximum Sensitivity Substrate (Thermo Fisher) was added to each sample and the luminescence was measured using a Glomax 20/20 Luminometer (Promega; Madison, WI) after a 10 second incubation.

HEK-293T cells were transfected with Kir6.2 constructs with or without a TAG stop codon corresponding to position 311. Cells were co-transfected with pANAP and eRF1-E55D in the presence or absence of SUR1 and cultured with or without ANAP. Wild-type Kir6.2-HA and Kir6.2-HA-GFP in the presence of SUR1 were included as positive controls. Kir6.2 constructs with no HA tag served as negative controls. In the presence of ANAP, we observed strong trafficking of Kir6.2*-HA-GFP to the plasma membrane, but much less trafficking of Kir6.2*-HA (Figure 1—Figure supplement 1E). When cells were cultured in the absence of ANAP, we observed little to no Kir6.2 surface expression from cells that were transfected with Kir6.2-W311^{TAG}-HA

or Kir6.2-W311^{TAG}-HA-GFP, suggesting that prematurely truncated constructs did not traffic to the plasma membrane. In the absence of SUR1, surface expression was weak for both wild-type and tagged constructs, despite the reported ability of Kir6.2-GFP to traffic to the plasma membrane in the absence of SUR1.

2.6 Epifluorescence imaging and spectroscopy

Epifluorescence imaging and spectroscopy were performed using a Nikon Eclipse TE2000-U microscope with a 60x water immersion objective (Plan Apo VC, NA = 1.2, Nikon; Kingston upon Thames, UK) or a 100x oil immersion objective (Nikon, Apo TIRF, NA = 1.49). Imaging of ANAP was performed using a 385 nm LED source (ThorLabs; Newton, NJ) with a 390/18 nm band-pass excitation filter, an MD416 dichroic and a 479/40 nm band-pass emission filter (all from ThorLabs). GFP was imaged using a 490 nm LED source (ThorLabs) with a 480/40 nm band-pass excitation filter, a DM505 dichroic, and a 510 nm long-pass emission filter (all from Chroma; Bellows Falls, VT). Fluorescence spectra were collected by exciting ANAP as above but using a 400 nm long-pass emission filter (ThorLabs), then passing emitted light through an IsoPlane 160 Spectrometer (Princeton Instruments; Trenton, NJ) with a 300 g mm⁻¹ grating. Images were collected with 1 s exposures on a Pixis 400BR_eXcelon CCD (Princeton Instruments).

2.7 Electrophysiology.

Patch pipettes were pulled from thick-walled borosilicate glass capillaries (GC150F-15, Harvard Apparatus; Holliston, MA) to a resistance of 1.5 MΩ to 2.5 MΩ when filled with pipette solution. Currents were recorded at -60 mV from excised inside-out patches using an Axopatch 200B amplifier equipped with a Digidata 1322A digitizer and using pClamp 10 software (Molecular Devices; San Jose, CA). Currents were low-pass filtered at 5 kHz and digitized at 20 kHz. The bath solution (intracellular) contained 140 mM KCl, 10 mM HEPES, 1 mM EDTA and 1 mM EGTA (pH 7.3 with KOH). The pipette solution (extracellular) contained 140 mM KCl, 10 mM HEPES

and 1 mM EDTA (pH 7.4 with KOH). All experiments were carried out in Mg²⁺-free conditions. Currents were leak corrected using the current remaining in bath solution containing 5 mM barium acetate at 60 mV, assuming a linear leak with a reversal potential of 0 mV. Inhibition was calculated and corrected for rundown by alternating test concentrations of nucleotide solution with nucleotide-free solution, then expressing the test currents as a fraction of the average of the control currents before and after the test solution as described previously.

2.8 FRET calculations

We calculated the expected FRET efficiency between ANAP incorporated at amino acid position 311 and a docked TNP-ATP molecule as described previously. The equivalency between FRET efficiency (measured as ANAP quenching) and nucleotide binding is based on two main assumptions. Firstly, we assume that the observed quenching from a bound nucleotide does not differ dramatically between open and closed states of the channel. As there is no open-state structure of K_{ATP}, we do not know exactly how much relative movement would occur between a bound TNP-ATP and Kir6.2-W311. However, based on cryo-EM structures of apo and nucleotide-bound Kir6.2 we do not expect to see a change in the distance between these two positions.

Secondly, we assume that the ANAP and TNP-ATP molecules on each subunit do not undergo energy transfer with those on other subunits to an extent which would dramatically change the observed quenching. At saturating TNP-ATP concentrations, where each ANAP-labelled site on Kir6.2 is occupied, FRET between ANAP and the closest acceptor will be kinetically favoured and the overall FRET efficiency will not be affected by cross-talk between neighbouring sites. In the limiting case, at low TNP-ATP concentrations, one would expect a large proportion of Kir6.2 tetramers (with four ANAP-labelled binding sites) bound to only a single TNP-ATP molecule. In this case, we expect a 4% overestimation of nucleotide binding as calculated using a numerical method to simulate a single TNP-ATP acceptor with multiple ANAP donors based on the distances calculated from our docking. This may have resulted

in our binding curves becoming artificially shallow at low concentrations. However, this difference is not significant in the context of our measurements as it is smaller than the observed error of our measurements at low TNP-ATP concentrations.

2.9 Unroofed binding measurements.

Unroofed membranes were prepared as described previously. A coverslip plated with transfected HEK-293T cells was removed from the culture media and rinsed with PBS. The coverslip was then briefly sonicated using a probe sonicator (Vibra-cell; Newtown, CT) leaving behind adherent plasma membrane fragments. Cells cultured on FluoroDishes were rinsed and sonicated directly in the dish. Unroofed membrane fragments were nearly invisible in bright-field images and identified by their GFP and ANAP fluorescence. Fluorescent TNP-nucleotides (Jena Bioscience; Jena, Germany) were diluted in bath solution and perfused onto unroofed membranes using a valve controlled microvolume superfusion system (μ Flow, ALA Scientific Instruments; Farmingdale, NY).

Fluorescence spectra were collected as described above. A region of interest corresponding to the membrane fragment was manually selected and line-averaged for each wavelength. A similarly sized region of background was selected and averaged, then subtracted from the spectrum of interest. After subtraction, ANAP intensity was calculated by averaging the fluorescence intensity measured between 469.5 nm and 474.5 nm. Bleaching was corrected by fitting the normalised ANAP intensity of exposures taken during perfusion with nucleotide-free solution to a single exponential decay of the form

$$\frac{F}{F_{max}} = ae^{kt} + (1 - a) \quad (2.1)$$

then using the fit to correct the intensity of exposures taken during perfusion with test nucleotide solutions.

Some experiments were excluded from further analysis due to obvious cross-contamination between different solutions within the μ Flow superfusion system.

These were identified by noticeable colour changes in the solution in the delivery tubes.

2.10 Patch-clamp fluorometry.

The tip of the patch pipette was centred on the slit of the spectrometer immediately after patch excision. Currents were measured as described above. Fluorescence emission spectra from the excised patch were acquired concurrently with current measurements, both during test solution application as well as nucleotide-free solution. Background subtraction was slightly imperfect due to the exclusion of TNP-ATP from volume of the glass of the pipette, resulting in spectra that have negative intensities at the TNP-ATP peak at high nucleotide concentrations. However, this over-subtraction does not affect the size of the ANAP peak, which we used to quantify nucleotide binding.

ANAP bleaching was corrected as for the unroofed binding experiments with Equation 2.1 (Figure 2-Figure supplement 3A). Due to the lower signal-to-noise ratio for PCF compared to the unroofed membranes, we performed experiments from both high-to-low and low-to-high TNP-ATP concentrations to minimise artifacts from our bleaching corrections. Kir6.2*-GFP + SUR1 showed consistent bleaching time courses (Figure 2-Figure supplement 3B) and an average of 34% of the initial ANAP fluorescence intensity remained at the end of each experiment (Figure 2-Figure supplement 3C).

Some experiments were excluded from further analysis due to low fluorescence intensity, as we were concerned about a low signal to noise ratio influencing our results.

2.11 Data processing and presentation.

Raw spectrographic images and current traces were pre-processed in Python and Clampfit (Axon) before analysis with R. Where applicable, all experimental data points are displayed in each figure. The number of experiments is reported in the

figure legends and tables. To help visualise uncertainty and prevent some data points being hidden, they are arranged with a small amount of horizontal jitter; vertical position remains unaffected. Unless otherwise stated, summary statistics are overlaid as the mean with error bars representing the standard error of the mean. Where these error bars are not visible, they are smaller than the size of the point used for the mean.

Hill fits to fluorescence quenching were nonlinear least-squares fits to the following equation:

$$\frac{y}{y_{max}} = 1 - E_{max} + \frac{E_{max}}{1 + 10^{(EC_{50} - [TNPATP]) \cdot h}} \quad (2.2)$$

where y represents normalised fluorescence intensity and EC_{50} and $[TNPATP]$ are \log_{10} values. Current inhibition data were fit to the same equation but with y representing normalised current magnitude, IC_{50} instead of EC_{50} , and I_{max} instead of E_{max} .

2.12 Computational docking.

Computational docking of TNP-ATP into the nucleotide binding site of Kir6.2 was performed using AutoDock-Vina and Pymol (Schrödinger, LLC; New York, NY). 11 TNP-ATP structures from the Protein Data Bank (PDB accession #s 1I5D, 3AR7, 5NCQ, 5SVQ, 5XW6, 2GVD, 5A3S, 2PMK, and 3B5J) were used as starting poses and a 15x11.25x15 Å box was centred on the ATP bound to Kir6.2 in PDB accession #6BAA. Protonation states for each residue were assigned using PDB2PQR and PROPKA 3.0. The modal highest-scoring pose from the docking run was selected (PDB accession #5XW6) and distances were measured from a pseudo atom at the centre of the fluorescent moiety. TNP-ATP (PDB #3AR7) was positioned into the first nucleotide binding domain of SUR1 (PDB #6PZI) using the alignment tool in Pymol.

2.13 Chemicals and stock solutions.

Unless otherwise noted, all chemicals were obtained from Sigma. TNP-ATP was obtained as a 10 mM aqueous stock from Jena Bioscience and stored at –20 °C. 1 mM aqueous stocks of ANAP-TFA were prepared by dissolving the free acid in 30 mM NaOH, and were stored at –20 °C. Tolbutamide stocks (50 mM) were prepared in 100 mM KOH and stored at –20 °C.

3

Measuring nucleotide binding to K_{ATP}

Contents

3.1 Choosing a site to incorporate Anap	21
3.1.1 Scanning a region	21
3.1.2 Rational residues	22
3.2 Testing for membrane expression	22
3.2.1 Expression with SUR1	22
3.2.2 Expression alone/with TMD0(195/232)	23

3.1 Choosing a site to incorporate Anap

Needs to fulfill a number of criteria:

Close enough to the binding site to measure FRET. Far enough from other classes of binding site to avoid interference. Far enough from other subunits to avoid cross talk.

3.1.1 Scanning a region

Introduced cutting sites and pasted in oligos (with Mike and Tascia - Mike did the molecular biology on SUR, I did on Kir6.2, Mike and I did surface expression together, Tascia did ephys on the mutants that expressed).

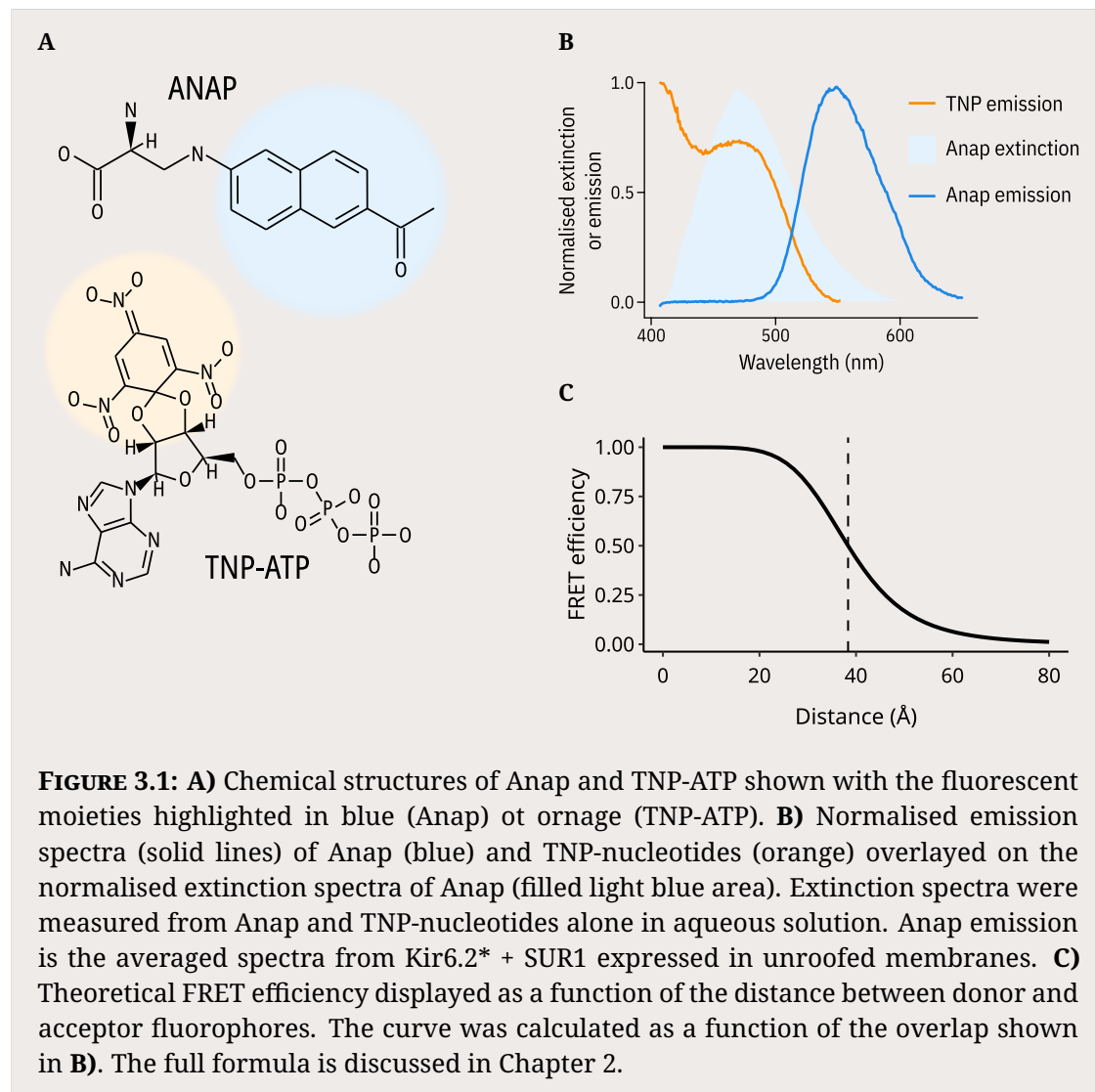


FIGURE 3.1: **A)** Chemical structures of Anap and TNP-ATP shown with the fluorescent moieties highlighted in blue (Anap) or orange (TNP-ATP). **B)** Normalised emission spectra (solid lines) of Anap (blue) and TNP-nucleotides (orange) overlayed on the normalised extinction spectra of Anap (filled light blue area). Extinction spectra were measured from Anap and TNP-nucleotides alone in aqueous solution. Anap emission is the averaged spectra from Kir6.2* + SUR1 expressed in unroofed membranes. **C)** Theoretical FRET efficiency displayed as a function of the distance between donor and acceptor fluorophores. The curve was calculated as a function of the overlap shown in **B**). The full formula is discussed in Chapter 2.

3.1.2 Rational residues

Number of hydrophobic residues chosen and mutated. Checked with exiFret v2 (might put discussion of this in appendix)

3.2 Testing for membrane expression

3.2.1 Expression with SUR1

Surface expression assay

Confocal microscopy

Electrophys

3.2.2 Expression alone/with TMD0(195/232)

Surface expression assay

Confocal (not with TMD0s)

Electrophys (tolbutamide)

4

MWC model formulation

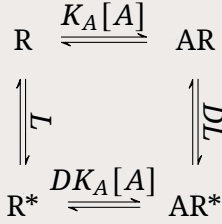
Contents

4.1 The MWC model	25
-----------------------------	----

4.1 The MWC model

The simplest case of an allosteric MWC model is shown in Figure 4.1. This simple case assumes a protein composed of a single monomer with a single binding site for ligand A. The protein is restricted to two states; R which is the inactive form and R* which is the active form. These two states exist in an equilibrium described by L, which is equivalent to $\frac{[R^*]}{[R]}$. Ligand A binds to the protein with a microscopic affinity constant K_A . However, the ligand A differentially stabilises the R and R* states by a constant D. When D is unity, the ligand A binds equally to both states and so does not influence the conformational changes of the protein. When $D > 1$, the ligand A preferentially stabilises the active R* state, while when $D < 1$ the ligand instead preferentially stabilises the inactive R state.

Two characteristics of interest - the equation for binding of ligand A and the equation for the probability of the protein being active - are shown in equations 4.2 and 4.3.

**FIGURE 4.1:** Single ligand, single protomer

$$[AR] = K_A[A][R] \quad [R^*] = L[R] \quad [AR^*] = DLK_A[A][R] \quad (4.1)$$

$$\begin{aligned} \frac{\text{bound}}{\text{all}} &= \frac{[AR] + [AR^*]}{[R] + [R^*] + [AR] + [AR^*]} \\ &= \frac{K_A[A][R] + DLK_A[A][R]}{[R] + L[R] + K_A[A][R] + DLK_A[A][R]} \\ &= \frac{K_A[A] + DLK_A[A]}{1 + L + K_A[A] + DLK_A[A]} \\ &= \frac{K_A[A](1 + DL)}{1 + K_A[A] + L(1 + DK_A[A])} \end{aligned} \quad (4.2)$$

$$\begin{aligned} \frac{\text{active}}{\text{all}} &= \frac{[R^*] + [AR^*]}{[R] + [R^*] + [AR] + [AR^*]} \\ &= \frac{L[R] + DLK_A[A][R]}{[R] + L[R] + K_A[A][R] + DLK_A[A][R]} \\ &= \frac{L + DLK_A[A]}{1 + L + K_A[A] + DLK_A[A]} \\ &= \frac{L(1 + DK_A[A])}{1 + K_A[A] + L(1 + DK_A[A])} \end{aligned} \quad (4.3)$$

If we consider introducing a second ligand B which binds to a distinct site and does not directly interact with ligand A, the scheme looks like Figure 4.2. Each ligand has its own microscopic association constant (K_A or K_B) and its own preference for the R or R* states (D_A or D_B). Importantly, there is no interaction term between ligand A and ligand B; the only way these ligands can impact each other is through effects on protein activity.

Similar equations for this more complicated model are shown here.

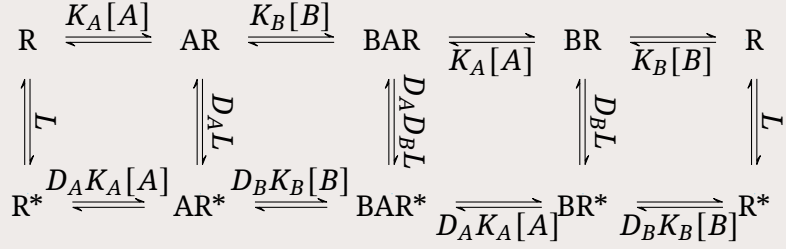


FIGURE 4.2: Two non-interacting ligands, single protomer

$$\begin{aligned}
[\text{AR}] &= K_A[\text{A}][\text{R}] & [\text{BR}] &= K_B[\text{B}][\text{R}] & [\text{BAR}] &= K_A[\text{A}]K_B[\text{B}][\text{R}] \\
[\text{R}^*] &= L[\text{R}] & [\text{AR}^*] &= LD_A K_A[\text{A}][\text{R}] & [\text{BR}^*] &= LD_B K_B[\text{B}][\text{R}] & [\text{BAR}^*] &= LD_A K_A[\text{A}]D_B K_B[\text{B}][\text{R}]
\end{aligned}$$

$$\begin{aligned}
\frac{\text{Abound}}{\text{all}} &= \frac{[\text{AR}] + [\text{AR}^*] + [\text{BAR}] + [\text{BAR}^*]}{[\text{R}] + [\text{R}^*] + [\text{AR}] + [\text{AR}^*] + [\text{BR}] + [\text{BR}^*] + [\text{BAR}] + [\text{BAR}^*]} \\
&= \frac{K_A[\text{A}][\text{R}] + LD_A K_A[\text{A}][\text{R}] + K_A[\text{A}]K_B[\text{B}][\text{R}] + LD_A K_A[\text{A}]D_B K_B[\text{B}][\text{R}]}{[\text{R}] + K_A[\text{A}][\text{R}] + K_B[\text{B}][\text{R}] + K_A[\text{A}]K_B[\text{B}][\text{R}] + L[\text{R}] + LD_A K_A[\text{A}][\text{R}] + LD_B K_B[\text{B}][\text{R}]} \\
&= \frac{K_A[\text{A}] + LD_A K_A[\text{A}] + K_A[\text{A}]K_B[\text{B}] + LD_A K_A[\text{A}]D_B K_B[\text{B}]}{1 + K_A[\text{A}] + K_B[\text{B}] + K_A[\text{A}]K_B[\text{B}] + L + LD_A K_A[\text{A}] + LD_B K_B[\text{B}] + LD_A K_A[\text{A}]D_B K_B[\text{B}]} \\
&= \frac{K_A[\text{A}](1 + LD_A) + K_A[\text{A}]K_B[\text{B}](1 + LD_A D_B)}{(1 + K_A[\text{A}])(1 + K_B[\text{B}]) + L(1 + D_A K_A[\text{A}])(1 + D_B K_B[\text{B}]})} \tag{4.4}
\end{aligned}$$

$$\begin{aligned}
\frac{\text{active}}{\text{all}} &= \frac{[\text{R}^*] + [\text{AR}^*] + [\text{BAR}^*] + [\text{BR}^*]}{[\text{R}] + [\text{R}^*] + [\text{AR}] + [\text{AR}^*] + [\text{BR}] + [\text{BR}^*] + [\text{BAR}] + [\text{BAR}^*]} \\
&= \frac{L[\text{R}] + LD_A K_A[\text{A}][\text{R}] + LD_B K_B[\text{B}][\text{R}] + LD_A K_A[\text{A}]D_B K_B[\text{B}][\text{R}]}{[\text{R}] + K_A[\text{A}][\text{R}] + K_B[\text{B}][\text{R}] + K_A[\text{A}]K_B[\text{B}][\text{R}] + L[\text{R}] + LD_A K_A[\text{A}][\text{R}] + LD_B K_B[\text{B}][\text{R}]} \\
&= \frac{L + LD_A K_A[\text{A}] + LD_B K_B[\text{B}] + LD_A K_A[\text{A}]D_B K_B[\text{B}]}{1 + K_A[\text{A}] + K_B[\text{B}] + K_A[\text{A}]K_B[\text{B}] + L + LD_A K_A[\text{A}] + LD_B K_B[\text{B}] + LD_A K_A[\text{A}]D_B K_B[\text{B}]} \\
&= \frac{L(1 + D_A K_A[\text{A}])(1 + D_B K_B[\text{B}])}{(1 + K_A[\text{A}])(1 + K_B[\text{B}]) + L(1 + D_A K_A[\text{A}])(1 + D_B K_B[\text{B}]})} \tag{4.5}
\end{aligned}$$

Appendices

